A Dual-Band Quad-Port Circularly Polarized MIMO Antenna Based on a Modified Jerusalem-Cross Absorber for Wireless Communication Systems

Asif Khan, Yejun He, *Senior Member, IEEE*, and Zhi Ning Chen, *Fellow, IEEE*

***Abstract*—A modified Jerusalem-cross absorber (MJCA) based on resistors is presented to minimize mutual coupling at two independent bands of a very compact quad-port multiple-input-multiple-output (MIMO) antenna. The double E-shaped radiating element features sectoral slots, enabling the antenna to function at two distinct frequencies: a lower band (LB) of 6.5 GHz and an upper band of 8.5 GHz. These slots also facilitate the conversion of linear to circular polarization, adding to the antenna's versatility and performance capabilities. The MJCA, composed of four resistors placed at right angles to each other with 150 Ω lumped resistances, provides an absorbance rate of more than 90%, and reflectivity tends to zero at both operating bands. The single antenna is modified into a 4 × 4 MIMO antenna, with all elements tilted up to 15° to improve impedance matching and increase isolation to some extent. Moreover, a 2 × 2 array of MCJA is placed on top of the MIMO antenna at a certain height, further enhancing isolation up to −35 and −25 dB at the 6.4–6.8 and 8.3–8.6 GHz frequency bands, respectively. In addition, it also improves the bandwidth of the MIMO antenna to up to 100 MHz at the LB. A detailed equivalent circuit design procedure is developed to understand the operating principles better. The designed MIMO antenna's performance with diverse parameters is also analyzed. The fabrication and measurement of the MIMO antenna validate the simulation results and demonstrate a good agreement between them. The proposed MIMO antenna is a competitive candidate for various modern wireless communication systems, including satellite communication, remote sensing, navigation systems, radar systems, and medical applications.**

***Index Terms*—Circular polarization, modified Jerusalem-cross absorber (MJCA), multiple-input-multiple-output (MIMO) antenna, mutual coupling.**

Manuscript received 26 May 2023; revised 22 September 2023; accepted 7 October 2023. Date of publication 26 October 2023; date of current version 9 February 2024. This work was supported in part by the National Key Research and Development Program of China under Grant 2023YFE0107900; in part by the National Natural Science Foundation of China under Grant 62071306; and in part by the Shenzhen Science and Technology Program under Grant JCYJ20200109113601723, Grant JSGG20210420091805014, and Grant JSGG20210802154203011. *(Corresponding author: Yejun He.)*

Asif Khan and Yejun He are with the State Key Laboratory of Radio Frequency Heterogeneous Integration, Sino-British Antennas and Propagation Joint Laboratory of MOST, Shenzhen Key Laboratory of Antennas and Propagation, Guangdong Engineering Research Center of Base Station Antennas and Propagation, College of Electronics and Information Engineering, Shenzhen University, Shenzhen 518060, China (e-mail: asifm20019@gmail.com; heyejun@126.com).

Zhi Ning Chen is with the Department of Electrical and Computer Engineering, National University of Singapore, Singapore 119077 (e-mail: eleczn@nus.edu.sg).

Color versions of one or more figures in this article are available at https://doi.org/10.1109/TAP.2023.3326285.

Digital Object Identifier 10.1109/TAP.2023.3326285

I. Introduction

THE use of circularly polarized (CP) multiple-input-multiple-output (MIMO) antenna arrays have become increasingly popular in modern wireless communication systems because CP MIMO antennas offer several transmission benefits such as a high-channel capacity, polarization mismatch immunity, and multipath interference resistance [1], [2], [3]. In engineering applications such as satellite and radar technology, adjacent elements in an array are typically spaced no more than half a wavelength apart to prevent grating lobes and meet practical requirements such as wide-angle scanning, high resolution, high signal-to-noise ratio, and space limitations. However, these high-density CP array configurations often encounter a significant challenge of intense mutual coupling among neighboring elements [4], leading to the arrays overall performance degradation. Developing an efficient decoupling structure for wideband high-density CP arrays is essential since interelement couplings can considerably affect array performance [5], [6]. Therefore, developing a decoupling framework that effectively reduces interelement couplings is greatly desired.

In recent decades, various studies have been conducted to enhance port-to-port isolation of multi-port antennas [7]. The utilization of a T-shaped decoupling structure on the ground plane has been employed as a technique to improve the isolation of multi-port antennas, as reported in [8]. This method has proven to be effective in increasing isolation by over 30 dB since it prevents the electric field from propagating from one element to the other. Another method involves a self-decoupling technique with two capacitive loads [9]. These techniques involve the use of either distributed [10], [11], or lumped decoupling networks placed behind the radiators to provide decoupling [12]. Similarly, by placing various structures between adjacent radiators, such as electromagnetic bandgap (EBG) structures [13], irregular parasitic element [14], defected ground structure (DGS) [15], neutralization lines [16], metamaterial (MTM) structures [17], artificial periodic metal strips [18], and meta-material is inspired to improve isolation [19]. Additionally, isolation is improved by a modified antenna decoupling surface (MADS), an H-shaped DGS (HDGS) with a decoupling structure [20], and field correlation reduced by employing a phase-gradient surface such as a superstrate in Fabry–Perot antennas [21]. However, most methods for reducing mutual coupling focus on linearly polarized (LP) arrays.

Circularly polarized arrays face a more significant challenge in reducing mutual coupling because it is essential to maintain a high-quality axial ratio (AR) across the operational frequency bands to achieve optimal performance, which makes the design process more challenging than that of LP arrays. Several works have been recently issued to address this problem, such as a decoupling layer based on a transmission-type frequency selective surface (FSS) between two closely spaced CP MIMO antennas, as described in [22]. In [23], the authors utilized a single negative (SNG) MTM structure within the operational band to enhance the isolation between the radiators of a two-element CP conformal array. A W-shaped parasitic strip is created as a decoupling tool for a two-element CP array with simultaneous transmission and reception functions, as explained in [24]. Despite their effectiveness, these CP decoupling methods have inherent drawbacks that limit their widespread applications, including relatively high profiles [22], complex 3-D structures with integration difficulties [23], and relatively narrow CP bandwidths [22], [23], [24]. While various techniques are used to reduce mutual coupling between dual-band antenna elements, one approach uses a metasurface superstrate which consists of pairs of nonuniform cut wires of different lengths positioned above the radiators [25]. Self-decoupling is another method used in a dual-band MIMO antenna [26]. Furthermore, two planar inverted-F antennas (PIFAs) have been arranged back-to-back. They are designed to operate independently at two different frequency bands, ensuring high isolation between them [27], [28]. MIMO antennas with closed slots [29], and decoupling networks [30] are suggested for dual-band operations but come with limitations and complexities. Consequently, achieving high isolation properties between the elements of a compact multi-band antenna system remains a considerable challenge.

To reduce mutual coupling in a dual-band quad-port MIMO antenna, a modified Jerusalem-cross absorber (MJCA) superstrate is suggested in the design proposal. The results demonstrate that significant isolation is achieved in both operational bands of the MIMO antenna, despite the limited edge-to-edge spacing of only 0.086λ at the lower band (LB). By utilizing the proposed MJCA superstrate, the isolation performance can be further enhanced to exceed -25 dB in both the LB and high band frequencies.

This work presents several contributions as follows.

1) Initially, a dual-band single antenna with bandwidths of 6.4–6.7 and 8.3–8.6 GHz is proposed. We design sectoral-shaped slots in a rectangular patch, resulting in a unique double E-shaped antenna. The addition of these sectoral slots also causes a change in the antenna's polarization behavior from linear to circular at both bands.
2) By tilting the feeding lines at different angles, the single antenna is converted into a quad-port MIMO antenna, resulting in the best impedance matching at 15° to reduce mutual coupling below -15 dB.

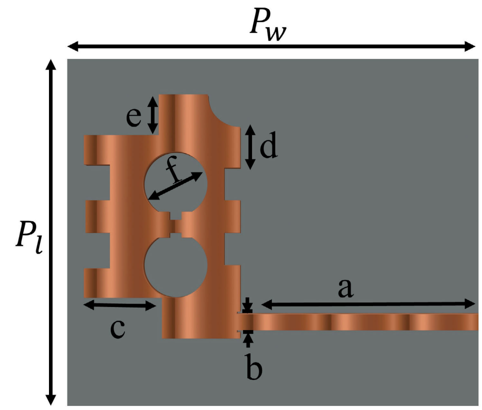

Fig. 1. Front view of the single antenna.

3) We introduce a novel technique for decoupling in an MIMO antenna that operates at two different frequency bands. The method involves tilting all the elements to a specific angle and utilizing a MJCA. This approach improves the bandwidth by up to 100 MHz in the LB and decreases the mutual coupling by up to 25 dB in both bands.

II. MIMO Antenna Design Procedure

A. Initial Antenna

A single antenna is designed using a low-cost $0.54\lambda \times 0.54\lambda \times 0.034\lambda$ FR-4 substrate with a relative permittivity of 4.4, and a dielectric loss tangent of 0.02 is given in Fig. 1. The antenna's geometry has transformed from a typical rectangular patch to integrating various shapes, such as two circles, a semicircle, and sectoral slots with rectangular shapes, as seen in Fig. 2(a). The resulting shape provides suitable impedance bandwidths and helps convert polarization from linear to circular in both desired bands.

The process of converting polarization in our proposed single-patch antenna design incorporates two techniques: perturbations and truncated corners. Perturbations consist of strategically placed cuts that influence the resonance create a 90° phase difference, resulting in circular polarization. Additionally, the introduction of truncated corners induces a phase difference during excitation, further enabling the transition to circular polarization. A microstrip feed line excites the antenna element with a matched impedance. An analysis of the changes made to the antennas structure and their impacts on the reflection coefficient and AR is presented in Fig. 2(b) and (c), respectively.

B. MIMO Antenna Configuration

Fig. 3 displays the proposed MIMO antenna, which is composed of four single antennas arranged in an orthogonal manner on a $1.08\lambda \times 1.08\lambda \times 0.034\lambda$ substrate. The interelement distance in this design is only 0.086λ at 6.5 GHz. The elements of the MIMO antenna are tilted at different angles to improve impedance matching and isolation, as shown in Fig. 3.

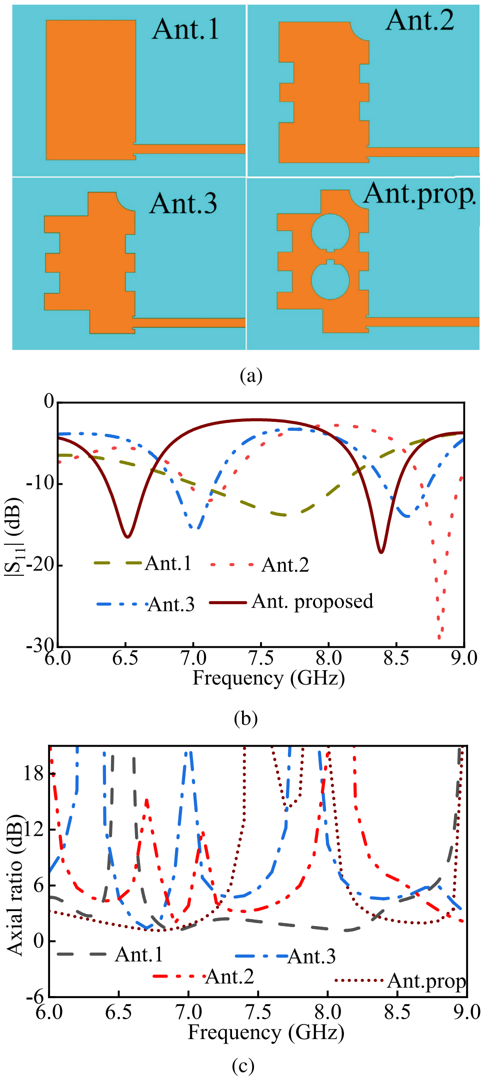

Fig. 2. (a) Designed iteration steps of the single antenna, (b) reflection coefficient, and (c) AR.

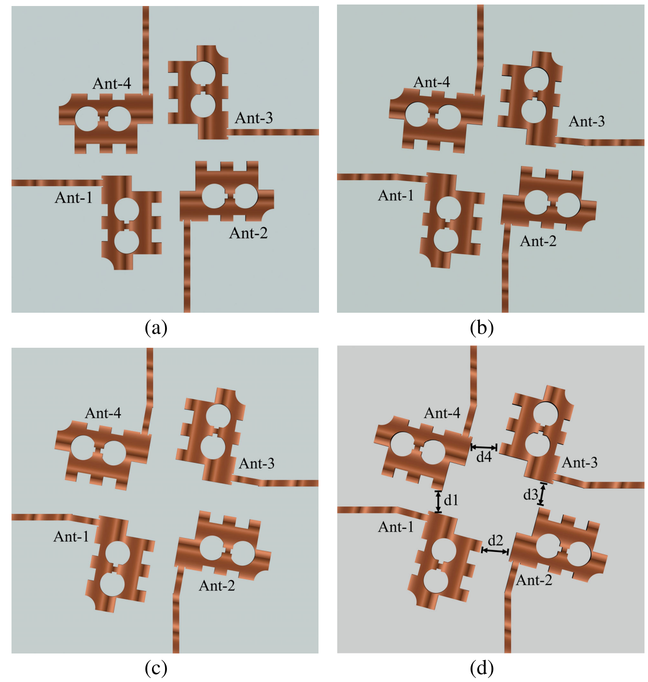

Fig. 3. Front view of the given MIMO antenna at different angles. (a) 0°, (b) 5°, (c) 10°, and (d) 15°.

According to the reflection coefficient values shown in Fig. 4(a), the reflection coefficient behavior of the MIMO antennas (S_{11}, S_{22}, S_{33}, and S_{44}) is not identical to that of a single-element antenna, with resonances occurring at different frequencies when the antennas are perpendicular to each other. Fig. 4(b) demonstrates that antenna-3 does not exhibit the same impedance bandwidth as the other three elements when the MIMO antennas are tilted to 5°. However, tilting all elements to 10° and 15°, as shown in Fig. 4(c) and (d), results in a better impedance bandwidth response in the 6.4–6.8 and 8.3–8.6 GHz frequency ranges. As a result, the MIMO antenna has an impedance bandwidth similar to that of the single antenna.

Fig. 5 presents the mutual coupling effects on the MIMO components and their optimal isolation. In Fig. 5(a), the isolation between antenna-1 and antenna-2 is presented at different angles, with −20 dB observed when the antennas are tilted up to 15° in both operating bands. As shown in Fig. 5(b), the minimum mutual coupling between antenna-1 and antenna-3 is less than −15 dB at a tilt of 15°. Fig. 5(c) presents the isolation between antenna-1 and antenna-4, where $|S_{14}/S_{41}|$ is greater than −15 dB at all degrees. These results indicate that the tilted MIMO antenna can increase isolation among the elements. However, the overall mutual decoupling in the proposed MIMO antenna is insufficient due to the close proximity of all elements.

A detailed parametric analysis focusing on the inter-element distance was carried out, as visualized in Fig. 6. The study evaluated five distinct distances, characterized by wavelengths ranging from 0.082λ to 0.090λ. Fig. 6(a) highlights the influence of different spacings among the patches on the reflection coefficient. It was observed that for most of the examined distances, the MIMO antenna consistently produced a bandwidth spanning from 6.35 to 6.48 GHz and from 8.25 to 8.45 GHz. However, an exception to this trend emerged when the patches were positioned at 0.086λ, indicating a distinctive response at this specific interelement spacing.

Fig. 6(b), (c), and (d) shows the port isolation variation across four elements with differing inter-element distances. It reveals that when the edge-to-edge distance stands at either 0.082λ or 0.084λ, there is high mutual coupling, approximately −10 dB, at both the lower and upper frequency bands, as shown in Fig. 6(b). In Fig. (c), by adjusting the interelement distance to 0.086λ for all antennas, the mutual coupling is reduced, achieving an isolation of less than −15 dB in both frequency bands. This configuration ensures optimal impedance matching and decreased mutual coupling among elements. On the other hand, by widening the space between elements, the isolation can be enhanced up to −17 dB, but only at the LB; it remains about −12 dB at the higher frequency band, specifically when the distance is set at 0.088λ or 0.090λ, as depicted in Fig. 6(d).

Our parametric analysis shows that an interelement distance of 0.086λ yields the most optimal results for both impedance matching and mutual coupling minimization. The dimensions

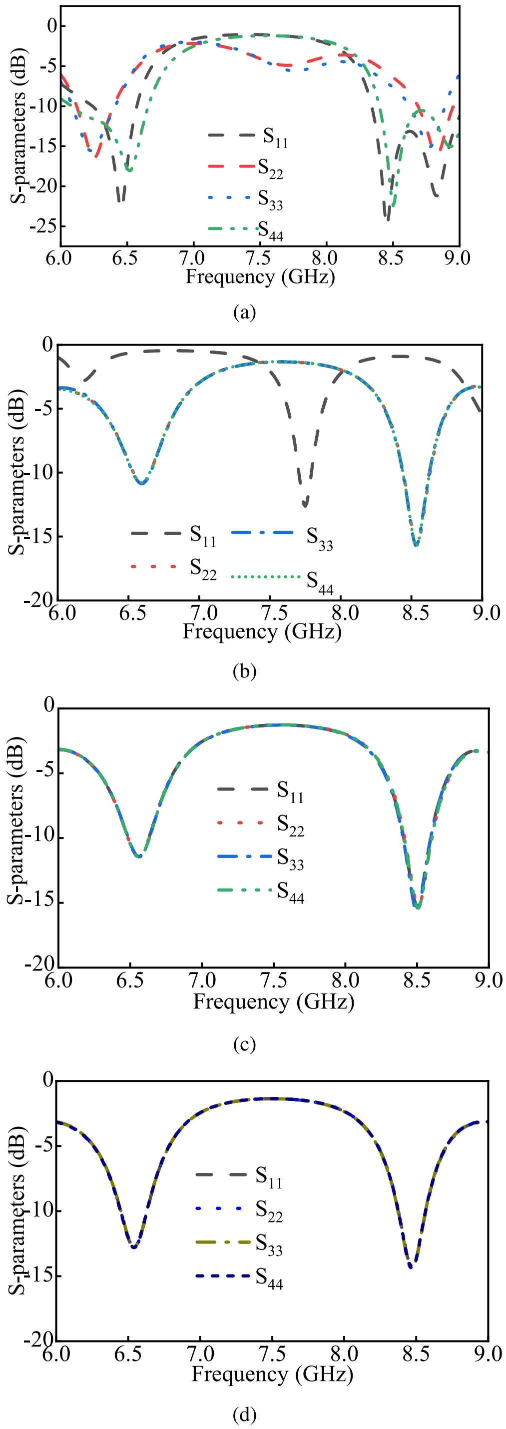

Fig. 4. Comparison of reflection coefficient when the projected MIMO antenna is placed at different angles. (a) 0°, (b) 5°, (c) 10°, and (d) 15°.

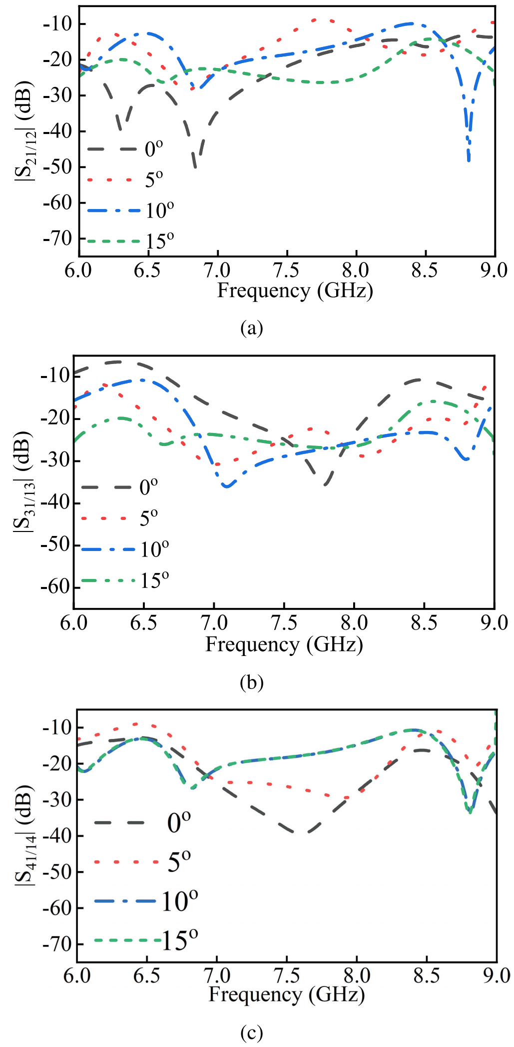

Fig. 5. Mutual coupling at different angles of the projected MIMO antenna. (a) $|S_{12}/S_{21}|$, (b) $|S_{13}/S_{31}|$, and (c) $|S_{14}/S_{41}|$.

TABLE I
DIMENSIONS OF THE PROPOSED SINGLE ANTENNA AND MIMO ANTENNA

Parameter	Value (mm)	Parameter	Value (mm)
P_l	20	P_w	25
a	12.3	b	1
c	4.8	d	1.8
e	2.5	f	4
d1	4.5	d2	4.5
d3	4.5	d4	4.5
L_p	50	W_p	50
H_p	3.5		

of the single antenna and proposed MIMO antenna are given in Table I.

C. Absorber Structure and Its Equivalent Circuit Design

The evolution steps of the proposed MJCA are depicted in Fig. 7(a)–(c). It is positioned on a Rogers RT/duroid 5880[1] with permittivity 2.2 and tan (loss tangent) = 0.0009 of 2.54 mm substrate height. The first step involved loading a simple Jerusalem-cross-shaped unit cell, as presented in Fig. 7(a). In the second step, four T-shaped bulges are added to the unit cell, as shown in Fig. 7(b). Finally, in the third step, four resistors (r_1, r_2, r_3, r_4) are added to the unit cell, each with a resistance of 150 Ω, as seen in Fig. 7(c). Meanwhile, the bottom of the substrate lacks any copper or conductor material to enable the electromagnetic current from the antenna to flow through to the superstrate. It is simulated by ANSYS HFSS using periodic-boundary conditions and the Floquet-port excitation. 2 × 2 unit cells of the MJCA are arranged on a superstrate, as shown in Fig. 7(d). The magnitude of the reflection coefficient of all the evolution

[1]Trademarked.

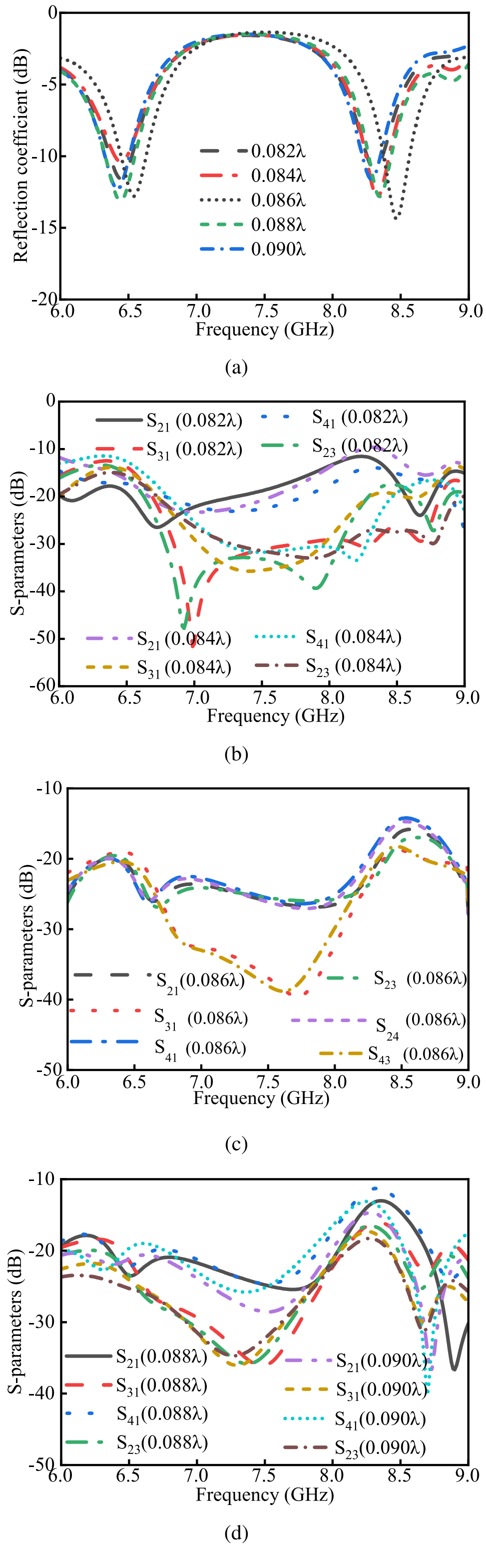

Fig. 6. Effects of the inter-element distance on the MIMO antenna's elements. (a) Reflection coefficient, while (b)–(d) transmission coefficient at different inter-element distances.

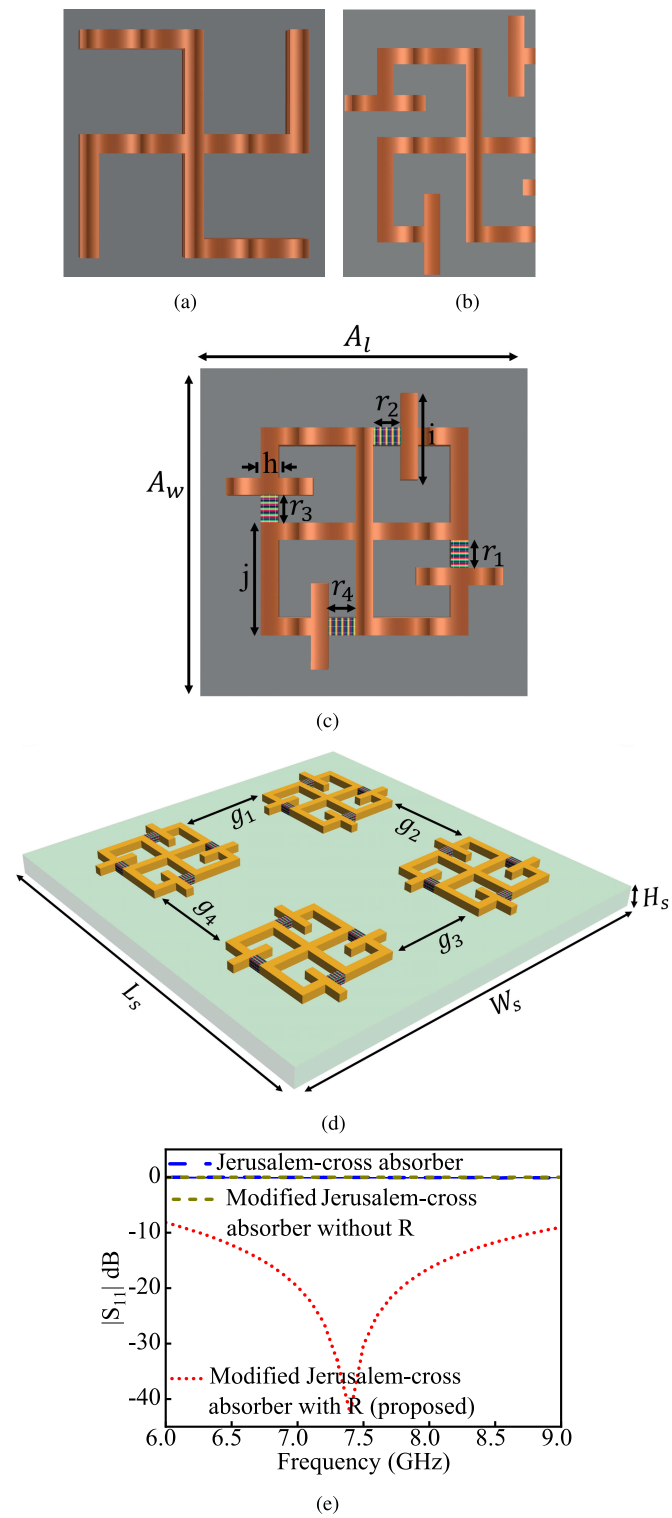

Fig. 7. (a) Jerusalem-cross absorber, (b) MJCA without R, (c) MJCA with R (proposed), (d) 2 × 2 absorbers of the MJCA, and (e) $|S_{11}|$ of all the evolutional steps.

steps is shown in Fig. 7(e). Without resistors, the absorber remains inert, not functioning at any frequency. However, integrating four resistors, each with a value of 150 Ω, implants the structure with functionality, enabling it to absorb electromagnetic waves efficiently. This setup yields a remarkable operational bandwidth of 3 GHz, spanning from 6 to 9 GHz. This wide frequency range, evidenced in Fig. 7(e), highlights the potential applications of this absorber in fields that require effective wide-band absorption. The dimensions of the MJCA are seen in Table II.

TABLE II
DIMENSIONS OF THE MJCA

Parameter	Value (mm)	Parameter	Value (mm)
A_l	25	A_w	25
h	1	r_1	1.6
r_2	1.6	r_3	1.6
r_4	1.6	j	6.5
L_s	25	W_s	25
H_s	2.54	g_1	13
g_2	13	g_3	13
g_4	13		

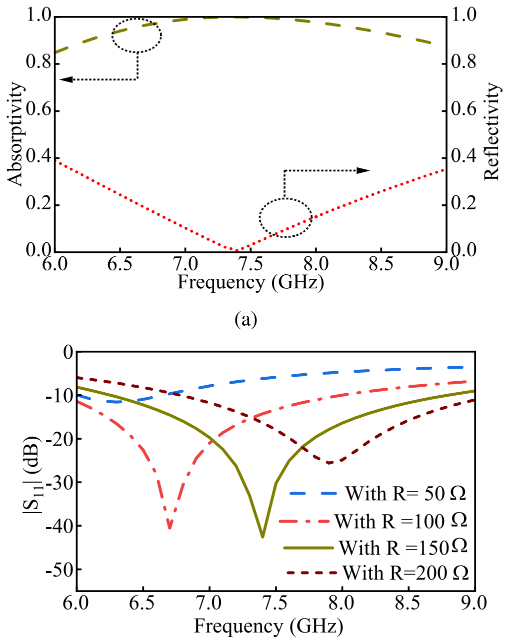

(a)

(b)

Fig. 8. (a) Absorptivity and reflectivity and (b) $|S_{11}|$ of the proposed absorber unit cell as a function of the lumped resistance values.

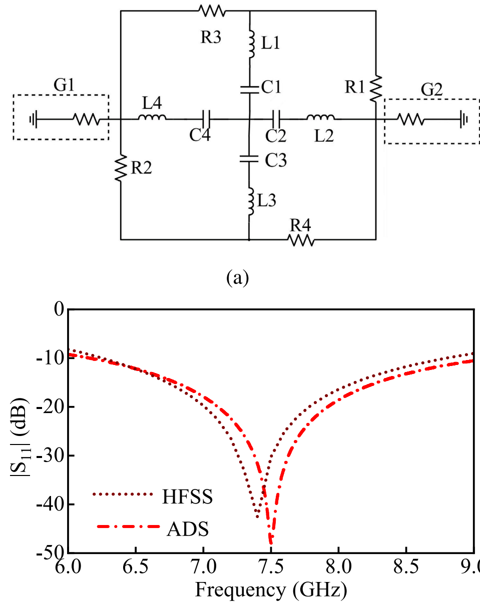

(a)

(b)

Fig. 9. (a) Generalized ECM presented for the MTM and (b) comparison of $|S_{11}|$ between simulated and ECM.

TABLE III
OPTIMIZED *RLC* FOR THE MJCA ECM

Parameter	Value	Parameter	Value
L_1	1 nH	L_2	1 nH
L_3	1 nH	L_4	1 nH
C_1	450 fF	C_2	450 fF
C_3	450 fF	C_4	450 fF
R_1	150 Ω	R_2	150 Ω
R_3	150 Ω	R_4	150 Ω

The absorptivity *"A"* of the proposed MJCA structure can be calculated by [31]

$$A = 1 - |S_{11}|^2 - |S_{21}|^2. \tag{1}$$

The reflectivity and transmissivity of the MTM surface to frequency are represented by $|S_{11}|^2$ and $|S_{21}|^2$, respectively. The absorption curve depicted in Fig. 8(a) demonstrates that the MTM surface can absorb above 90% of the electromagnetic waves within a bandwidth ranging from 6 to 9 GHz, covering both operating bands. The absorption bandwidth defines the range of frequencies in which the MTM surface can absorb the incident radiation. As a result, the MTM absorbers bandwidth limits the reduction in mutual coupling between antennas. The resistor-inductor-capacitor (*RLC*) values of the MJCA are shown in Table III.

Fig. 8(b) provides the parametric variation of S_{11} at different values of the loaded lumped resistance for the intended frequency of the proposed unit cell. This proves the ability of the proposed design to adapt to changes in absorbance, when the proposed absorber adopted lumped resistances of $R_{1,2,3,4} = 50$, 100, 150, and 200 Ω. When the values of these resistors are shifted from 50 to 200 Ω, the lumped resistances had a slight effect on absorption in the operating frequency band, as shown in Fig. 8(b). Hence, by selecting a proper value for $R_{1,2,3,4} =$ 150 Ω, the proposed absorber provides excellent absorbance and reflectivity across the bandwidth from 6 to 9 GHz, making it the optimal value for the proposed design.

An equivalent circuit model (ECM) for the projected absorber is modeled and simulated using advanced design system (ADS) software, as illustrated in Fig. 9(a). The circuit comprises two conductance elements: G1 (represents the radiation conductance of the antenna) and G2 (represents the measure of the loss conductance due to ohmic loss, dielectric loss, and mismatch loss), an *RLC* circuit, where inductors, capacitors, and resistors were connected in series, as shown in Fig. 9(a). The inductors (L_1, L_2, L_3, and L_4) represent the unit cell's conducting part. In contrast, the capacitors (C_1, C_2, C_3, and C_4) represent the cuts or air gaps between adjacent conductors within the unit cell. Furthermore, four resistors of 150 Ω are incorporated into the circuit to represent the resistance of a conducting material. By adjusting the values of the inductors and capacitors, desired results comparable to those obtained using HFSS can be achieved. For the proposed unit cell, the reflection coefficient values between the simulated and ECMs demonstrate good agreement, as seen in Fig. 9(b).

D. MIMO Antenna Configuration With Superstrate Absorber

Fig. 10(a) describes the proposed geometric configuration of the MIMO antenna based on the MJCA superstrate. An array

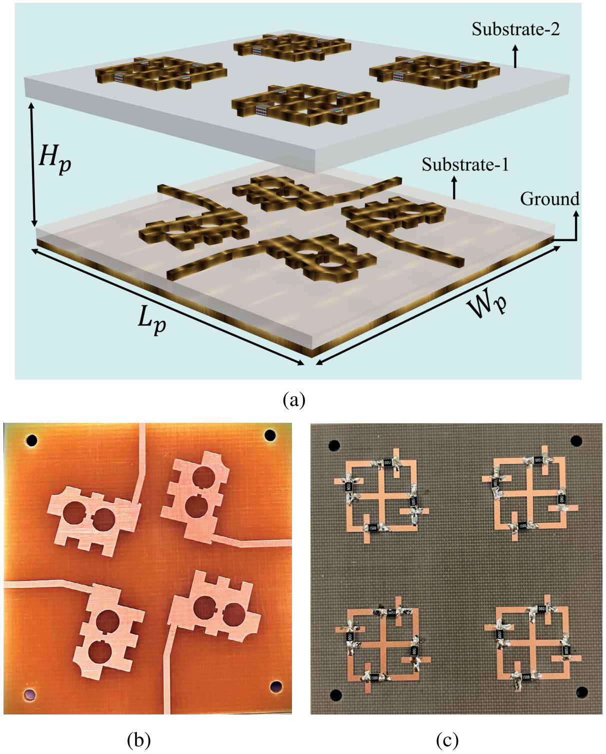

Fig. 10. (a) Schematic view of the proposed MIMO antenna, (b) photograph of fabricated prototype MIMO antenna layer, and (c) superstrate layer.

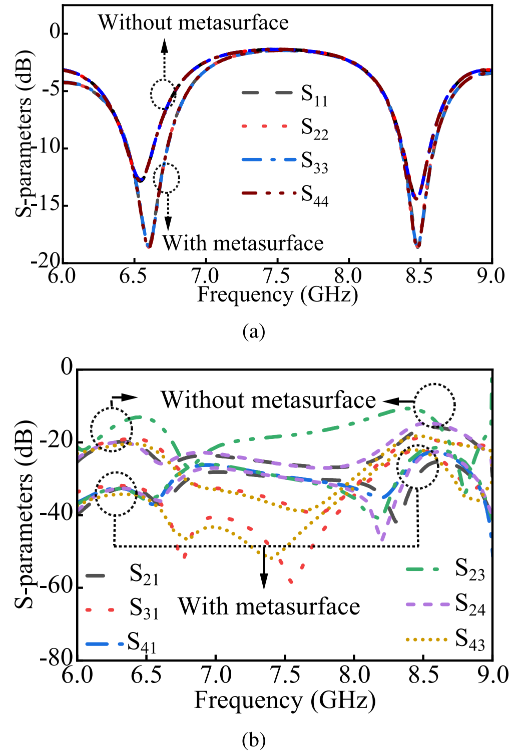

Fig. 11. (a) Reflection coefficient of the proposed MIMO antenna without and with superstrate and (b) mutual coupling without and with superstrate.

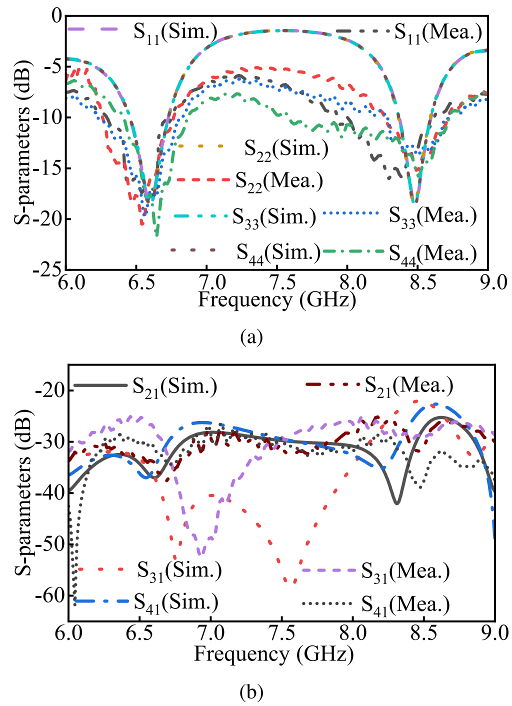

Fig. 12. Comparison between the simulated and measured results. (a) Reflection coefficient and (b) mutual coupling.

of 2 × 2 MJCAs, with dimensions of $0.1\lambda \times 0.1\lambda \times 0.052\lambda$, is designed and placed on top of the MIMO antenna at a height of 0.058λ. This height is determined after extensive parametric studies, considering various parameters, including bandwidth, isolation, and AR. Therefore, the MJCA array is utilized to improve the performance of the MIMO antenna system at this specific height. This is achieved by decreasing mutual coupling and amplifying the constructive interference between the waves generated by the antenna and those reflected by the superstrate. Fig. 10(b) and (c) demonstrate the front view of the fabricated MIMO antenna and superstrate, respectively.

The integration of the MJSCA has resulted in a substantial enhancement in the performance of the MIMO antenna, as demonstrated in Fig. 11(a) and (b). Fig. 11(a) displays the reflection coefficient graphs of the MIMO antenna, highlighting the variations in the absorber's LB pre- and post-utilization. The introduction of the absorber has resulted in a 100 MHz expansion in the impedance bandwidth, with the bandwidth now ranging from 6.7 to 6.8 GHz in the LB. In Fig. 11(b), the transmission coefficients curve depicts the minimum isolation among all antennas without metasurface, which is approximately −18 and −15 dB in both operating bands, respectively. Conversely, the transmission coefficient curves in Fig. 11(b) demonstrate the mutual coupling among all antennas with a metasurface, displaying a minimum isolation of −35 dB in the frequency band of (6.4–6.8 GHz) and −25 dB in the (8.3–8.6 GHz) band, respectively. Fig. 12(a) and (b) compare the simulated and measured S-parameters of the proposed MIMO antenna. The experimental results indicate that the mutual coupling in the MIMO antenna has been efficiently reduced while simultaneously achieving good matching performance at both frequency bands.

E. Gain and AR

A comparison between the simulated MIMO antenna gain with and without the integration of the metasurface at both operating bands is given in Fig. 13(a). The results indicate that

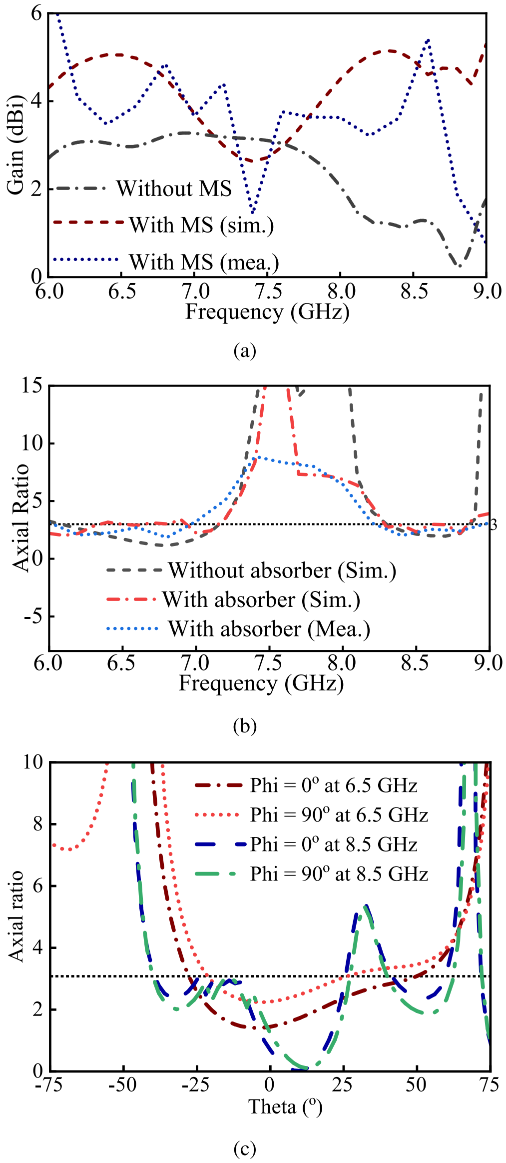

Fig. 13. (a) Comparison of simulated and measured gain for the proposed MIMO antenna, with and without a superstrate, (b) simulated and measured AR for the MIMO antenna, both without and with the superstrate, and (c) AR in the planes of phi = 0° and phi = 90°, at 6.5 and 8.5 GHz, respectively.

after adding the metasurface, the gain of the antenna system increases by approximately 3 dBi at both operating bands. The MJCA array operates as a superstrate layer that induces a resonant cavity effect, which leads to an increase in the gain of the antenna system. Additionally, Fig. 13(a) depicts a comparison between the simulated and measured results, highlighting their coherence.

The AR plays a critical role in determining the proposed antenna's circular polarization performance. To assess the influence of the MTM superstrate on CP characteristics, a comparative analysis is presented in Fig. 13(b), contrasting the antenna's performance with and without the integration of the MTM.

As previously discussed in the manuscript, the original MIMO antenna design already exhibits circular polarization due to the incorporation of multiple cuts in the single patch. This intrinsic design feature ensures satisfactory CP performance.

Following the integration of the MTM superstrate, a slight modification in the AR is observed across both frequency bands. Importantly, however, the AR remains consistently below 3 dB, affirming that the MIMO antenna retains its circularly polarized nature even with the inclusion of the superstrate. These results indicate the robustness of the proposed antenna design, which effectively preserves CP characteristics despite the presence of the MTM.

Furthermore, the comparison between the simulated and measured results of the MIMO antenna's AR, as presented in Fig. 13(b), exhibits a remarkable agreement. This validation underscores the accuracy and dependability of our antenna design, confirming that the simulation results accurately depict the actual performance of the antenna.

The angular range where the antenna's performance maintains under a specific threshold is defined by the 3-dB AR beamwidth. Fig. 13(c) depicts the simulated AR beamwidth of the proposed MIMO antenna at 6.5 GHz, specifically in the phi = 0° and phi = 90° planes. The 3-dB AR beamwidth for the phi = 0° plane at 6.5 GHz ranges from −25° to 50°. This means that the antenna's AR stays within 3 dB of the reference value inside this angular range. Similarly, the beamwidth for the phi = 90° plane at 6.5 GHz spans from −20° to 25°.

Similarly, at 8.5 GHz, the phi = 0° plane exhibits a 3-dB AR beamwidth ranging from −40° to 25°. The beamwidth for the phi = 90° plane at the same frequency ranges from −20° to 25°.

F. Surface Current Distribution and Radiation Pattern

Fig. 14 depicts the effect of field variations in the MIMO antenna with and without metasurface. It is evident from the field behavior that the MJCA impedes the current flow toward the neighboring element. This technique offers the benefit of incorporating an extra component that does not negatively affect the antenna's performance. The MTM surface functions as an absorbing medium for shielding purposes. Furthermore, this approach does not necessitate any field control tuning, unlike other methods proposed in the literature.

The radiation patterns of the MIMO antenna for left-hand circular polarization (LHCP) and right-hand circular polarization (RHCP) are compared in Fig. 15(a) and (b), respectively, with and without the implementation of the MTM surface. The antenna exhibits LHCP radiation at both operating frequencies. The results demonstrate that the field pattern is almost identical in both cases, primarily due to the placement of the MJCA on top of the antenna structure, which does not interfere with the radiation pattern. Consequently, the MIMO antenna can maintain its original radiation pattern while taking advantage of the MTM absorber's ability to reduce mutual coupling and increase gain. The simulated and measured radiation patterns are well-matched, as given in Fig. 15(c) and (d) at LB and upper bands, respectively.

The prototype's radiation characteristics are measured in a microwave anechoic chamber, where it is positioned in the far-field of a transmitting antenna and mounted on a rotatable platform for versatile testing, as shown in Fig. 16.

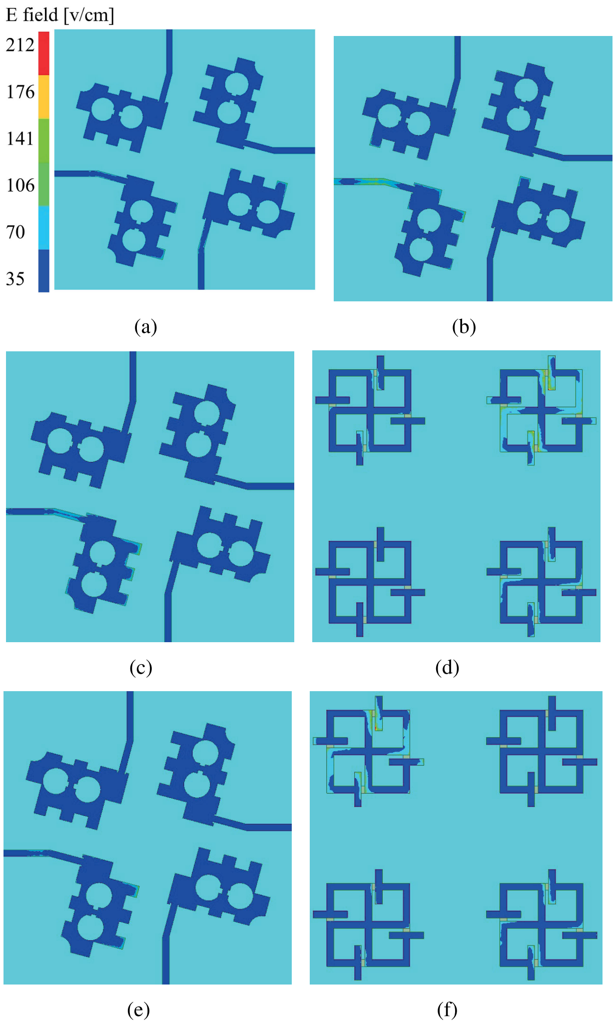

Fig. 14. Surface current distributions of the proposed MIMO antenna at (a) and (b) 6.5 and 8.5 GHz without the metasurface, (c) and (d) 6.5 GHz with the metasurface, and (e) and (f) 8.5 GHz with the metasurface.

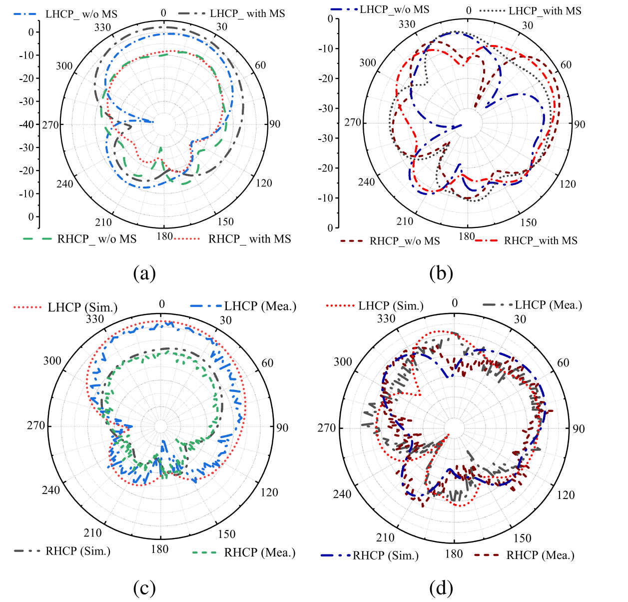

Fig. 15. Left-hand circularly polarized and right-hand circularly polarized radiation patterns. (a) and (b) LHCP and RHCP at 6.5 and 8.5 GHz without metasurface and (c) and (d) simulated and measured LHCP and RHCP at 6.5 and 8.5 GHz with metasurface.

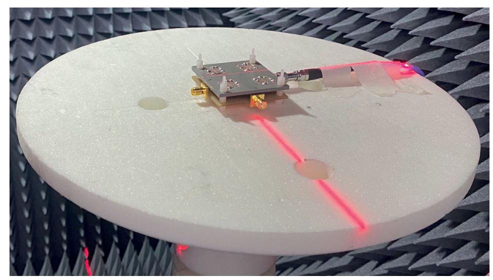

Fig. 16. Photograph of radiation pattern measurement.

III. Proposed MIMO Antenna's ECM

Fig. 17(a) illustrates a circuit model simulating a patch antenna designed to operate at two frequencies, 6.5 and 8.5 GHz. The model begins with a 50 Ω source. Following this, it incorporates two sets of components: one consisting of L_a and C_a for 6.5 GHz, and the other including L_b and C_b for 8.5 GHz. The components are connected in series (one after another) while their sets are connected parallel to feed the patch. The feeding network is connected to the antenna's radiating patch, where the signals are emitted, with a group of components (R_a, L_c, L_d, C_c, and C_d) arranged in parallel. For the proposed *RLC* circuit, the resonance frequencies of f_{c1} and f_{c2} are given by

$$f_{c1} = \frac{1}{2\pi\sqrt{L_1C_1}} = \frac{1}{2\pi\sqrt{L_2C_2}} \tag{2}$$

$$f_{c2} = \frac{1}{2\pi\sqrt{L_3C_3}} = \frac{1}{2\pi\sqrt{L_6C_6}} = \frac{1}{2\pi\sqrt{L_4C_4}}. \tag{3}$$

Tables V and VI provide the first and second resonance frequencies (f_{c1} and f_{c2}) for both ECM and calculated. Furthermore, the ECM bandwidths (BW_1 and BW_2) are determined as

$$BW_1 = \frac{fc1}{Q_1} = \frac{\frac{1}{2\pi\sqrt{L_1C_1}}}{\frac{1}{R\sqrt{\frac{L_1}{C_1}}}} = \frac{R_1}{2\pi L_1} \tag{4}$$

$$BW_1 = \frac{fc1}{Q_1} = \frac{\frac{1}{2\pi\sqrt{L_2C_2}}}{\frac{1}{R\sqrt{\frac{L_2}{C_2}}}} = \frac{R_1}{2\pi L_2} \tag{5}$$

$$BW_2 = \frac{fc2}{Q_2} = \frac{\frac{1}{2\pi\sqrt{L_3C_3}}}{\frac{1}{R\sqrt{\frac{L_3}{C_3}}}} = \frac{R_1}{2\pi L_3} \tag{6}$$

$$BW_2 = \frac{fc2}{Q_2} = \frac{\frac{1}{2\pi\sqrt{L_4C_4}}}{\frac{1}{R\sqrt{\frac{L_4}{C_4}}}} = \frac{R_1}{2\pi L_4}. \tag{7}$$

The values of both *RLC* circuit variables are shown in Table IV.

As depicted in Fig. 17(b), we have designed a circuit model of our proposed MIMO system. As previously mentioned, four-unit cells of the absorber are positioned at a specific height above the quad-port MIMO antenna to reduce mutual coupling. Regarding the circuit design, a 2 × 2 array of absorbers is placed centrally and connected in series. Subsequently, four distinct series connections are established from these absorbers to the four patches, each located at a

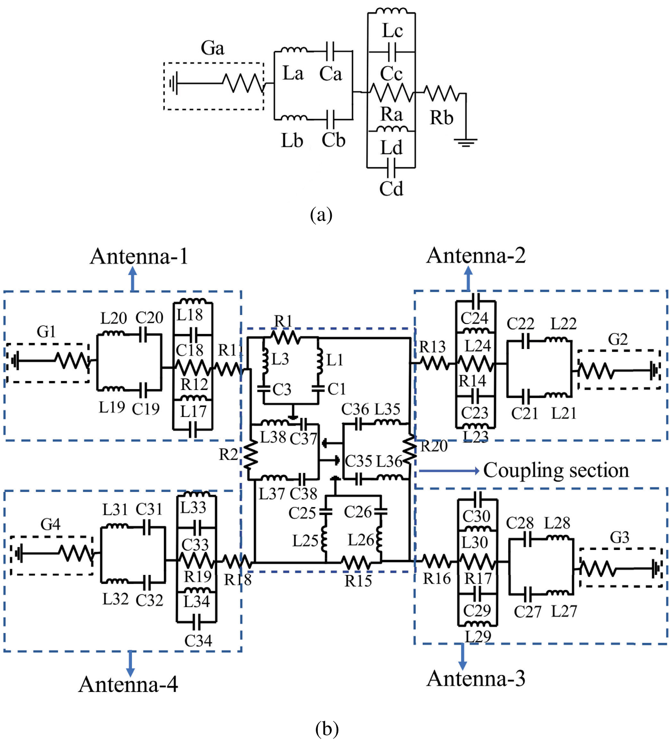

Fig. 17. (a) ECM of a single antenna and (b) MIMO antenna with the metasurface designed to enhance its performance.

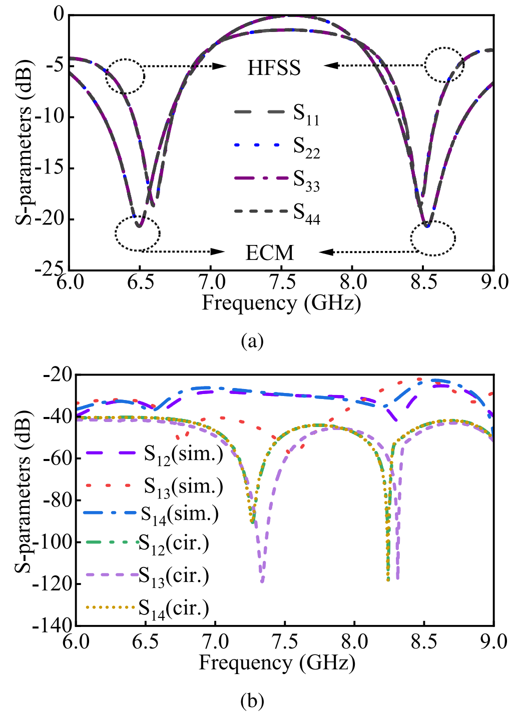

Fig. 18. S-parameter comparison between the simulated and the ECM of the projected MIMO antenna. (a) Reflection coefficient and (b) mutual coupling.

TABLE IV

OPTIMIZED *RLC* VALUES FOR THE SINGLE ANTENNA AND PROPOSED MIMO ANTENNA ECMS

Par.	value	Par.	value	Par.	value	Par.	value
L_a	0.2 nH	L_b	0.2 nH	C_1	350 fF	C_3	380 fF
L_c	0.2 nH	L_d	0.2 nH	C_{17}	29 fF	C_{18}	50 fF
C_a	50 fF	C_b	29 fF	C_{19}	29 fF	C_{20}	50 fF
C_c	50 fF	C_d	29fF	C_{21}	50 fF	C_{22}	29 fF
R_a	10 Ω	R_b	50 Ω	C_{23}	50 fF	C_{24}	29 fF
L_1	1 nH	L_3	1 nH	C_{25}	350 fF	C_{26}	380 fF
L_{17}	12 nH	L_{18}	12 nH	C_{27}	50 fF	C_{28}	19 fF
L_{19}	12 nH	L_{20}	12 nH	C_{29}	50 fF	C_{30}	29 fF
L_{21}	12 nH	L_{22}	12 nH	C_{31}	50 fF	C_{32}	29 fF
L_{23}	12 nH	L_{24}	12 nH	C_{33}	50 fF	C_{34}	29 fF
L_{25}	1 nH	L_{26}	1 nH	C_{35}	350 fF	C_{36}	380 fF
L_{27}	12 nH	L_{28}	12 nH	C_{37}	350 fF	C_{38}	380 fF
L_{29}	12 nH	L_{30}	12 nH	R_2	10 Ω	R_{11}	50 Ω
L_{31}	12 nH	L_{32}	12 nH	R_{12}	10 Ω	R_{13}	50 Ω
L_{34}	12 nH	L_{35}	1 nH	R_{14}	10 Ω	R_{15}	10 Ω
L_{36}	12 nH	L_{37}	1 nH	R_{16}	50 Ω	R_{17}	50 Ω
L_{38}	1 nH	R_1	10 Ω	R_{18}	50 Ω	R_{19}	10 Ω
R_{20}	10 Ω						

corner. This arrangement is designed to achieve our desired performance results.

The magnitudes of capacitors and inductors are modified to adjust the reflection coefficients of the proposed dual-band single antenna to the resonance frequencies. Fig. 18(a) shows a comparison of the mutual correlation between the reflection coefficients of the proposed dual-band antenna and the equivalent *RLC* circuit model. This comparison indicates an excellent level of agreement between them. According to the results presented in Tables V and VI, the values of L_a, L_c, C_a, and C_c are responsible for determining the first resonance frequency, whereas the values of L_b, L_d, c_b, and c_d are responsible for tuning the second resonance frequency. The first calculated resonance frequency (f_{c1}) values for the proposed ECMs are 6.53 and 6.5 GHz, respectively. Similarly, the second calculated resonance frequency (f_{c2}) values for the proposed ECMs are 8.53 and 8.5 GHz, respectively. The mutual coupling results of both the simulated and calculated circuit models show a good match, as displayed in Fig. 18(b).

IV. MIMO PARAMETERS ANALYSIS

In a multi-element system, determining the effective bandwidth only based on the scattering matrix is insufficient; thus, the envelope correlation coefficient (ECC), diversity gain (DG), total active correlation coefficient (TARC), and channel capacity loss (CCL) must also be considered [19]. The analysis depicted in Fig. 19(a) reveals that the proposed antenna demonstrates an ECC value below 0.075 at two distinct operating frequencies. This value is considered significantly low, obtained through evaluating ECC from far-field radiation patterns. Additionally, based on ECC, the proposed MIMO antenna achieves a DG of 9.9999 dBi at both frequencies, which is a significant accomplishment in diversity analysis. The simulated and measured results show only minor discrepancies within an acceptable range. Furthermore, based on the measured results, the TARC and CCL can be calculated. The TARC value averages at −22 and −25 dB for the 6.5 and 8.5 GHz bands, respectively. The CCL averages at 0.15 and 0.013 bits/sec/Hz for the lower and upper frequency bands, respectively, as presented in Fig. 19(b).

V. PERFORMANCE COMPARISON

Table VII compares the proposed decoupling and referenced techniques, highlighting the former's superiority. The proposed

TABLE V
LIST OF PARAMETERS ASSOCIATED WITH THE LB FREQUENCY f_{c1}

Parameter	L_a(nH)	C_a (fF)	L_c (nH)	C_c (fF)	f_{c1} calculated (GHz)	f_{c1} ECM (GHz)	BW_1 calculated (GHz)	BW_1 ECM (GHz
Value	0.2	50	0.2	50	6.53	6.5	480	460

TABLE VI
LIST OF PARAMETERS ASSOCIATED WITH THE UPPER BAND FREQUENCY f_{c2}

Parameter	L_b(nH)	C_b (fF)	L_d (nH)	C_d (fF)	f_{c2} calculated (GHz)	f_{c2} ECM (GHz)	BW_2 calculated (GHz)	BW_2 ECM (GHz
Value	0.2	29	0.2	29	8.53	8.5	480	470

TABLE VII
PERFORMANCES COMPARISON WITH OTHER DUAL-BAND MIMO ANTENNAS

Ref.	Method	Operating frequencies	Bandwidth improvement(dB)	Isolation (dB)	Interelement distance (λ_o)	Polarization	Gain enhancment (dBi)
[25]	MDM	2.6, 3.5	NA	25	0.008	Linear	NA
[26]	Self decoupling	6.5, 8	NA	17	0.015	Circular	NA
[27]	Defective ground structure	2.4, 5.5	NA	26	0	Linear	NA
[28]	Resonant structure and DGS	2.4, 5.5	NA	26.7	0.017	Linear	NA
[29]	Mode cancellation	2.4, 5	NA	15, 25	0.011	Linear	NA
[30]	Dual-band DMN	3.45, 4.9	NA	13,15	0.034	Linear	NA
This work	Tilting and MJ-CA	6.5, 8.5	100 MHz	35, 25	0.086	Circular	2 dBi, 3.5 dBi

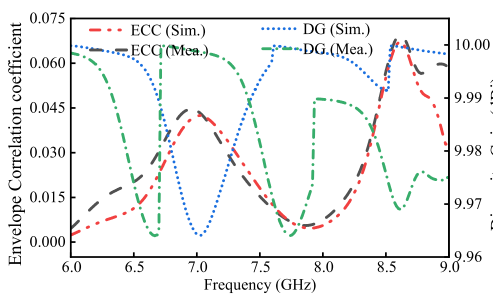

(a)

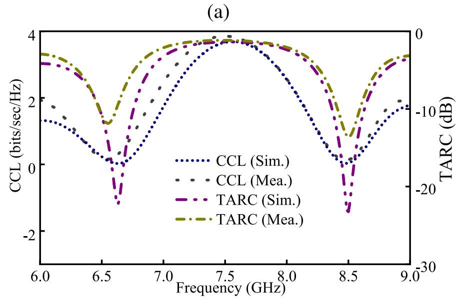

(b)

Fig. 19. Diversity analysis. (a) ECC from far-field radiation pattern and DG, (b) TARC, and CCL.

technique offers three distinct advantages over previous techniques, which are discussed and compared in Table VII.

A. Dual Band and Circular Polarization

Most of the previous techniques focus on dual-band LP antennas, except [26]. However, in the proposed MIMO antenna, sectoral slots are used to achieve dual-band capability by converting the linear polarization into circular polarization.

B. Reflection Coefficient and Mutual Decoupling Improvement

The prototype with a hybrid decoupling technique achieves a superior isolation of 35 and 25 dB over a frequency band of 6.4–6.8 and 8.3–8.6 GHz, respectively. Notably, this work provides a remarkable improvement in isolation at lower frequencies than previous techniques [26], [27], [30]. Furthermore, the proposed technique has resulted in a 100 MHz increase in impedance bandwidth in the LB.

C. Gain Enhancement

The manuscript shows that previous studies did not improve the gain of the antenna, while the proposed work has managed to enhance the gain by up to 2 and 3 dBi at the lower and higher frequency bands, respectively.

Although some of the structures in the literature are very compact [25], [26], [29], they tend to have complex designs. Therefore, the proposed antenna demonstrates superior performance compared to the existing literature.

VI. CONCLUSION

This article presents an MJCA with a multi-resistor configuration, arranged orthogonally. The proposed design minimizes mutual coupling in a compact dual-band four-element MIMO antenna. The patch includes several sectoral cuts that convert polarization from linear to circular. The results obtained from both simulation and measurement indicate a significant enhancement in isolation between any of the patch antennas, even when the edge-to-edge space between them is as small as 0.086λ. The proposed design achieves more than 25 dB of isolation at 6.4–6.8 and 8.3–8.6 GHz frequency bands. The designed antenna exhibits excellent diversity performance, including ECC, TARC, and CCL values of less than 0.025, -20 dB, and 0.15 bits/sec/Hz, respectively, at both bands. Meanwhile, it maximized DG up to 10 dBi due to low ECC. The article also includes an analysis of an ECM that provides a better understanding of the design. The antenna's circular polarization characteristic makes it an ideal choice for satellite communication systems, especially in challenging conditions.

REFERENCES

[1] L. Zhang et al., "Single-feed ultra-wideband circularly polarized antenna with enhanced front-to-back ratio," *IEEE Trans. Antennas Propag.*, vol. 64, no. 1, pp. 355–360, Jan. 2016.

[2] T. K. Nguyen, H. H. Tran, and N. N. Tong, "A wideband dual-cavity backed circularly polarized crossed dipole antenna," *IEEE Trans. Antennas Propag.*, vol. 66, no. 5, pp. 2675–2679, May 2018.

[3] W. Yang, Y. Pan, S. Zheng, and P. Hu, "A low-profile wideband circularly polarized crossed-dipole antenna," *IEEE Trans. Antennas Propag.*, vol. 66, no. 6, pp. 3327–3330, Jun. 2018.

[4] M. J. Al-Hasan, T. A. Denidni, and A. R. Sebak, "Millimeter-wave compact EBG structure for mutual coupling reduction applications," *IEEE Trans. Antennas Propag.*, vol. 63, no. 2, pp. 823–828, Feb. 2015.

[5] K. S. Vishvaksenan, K. Mithra, R. Kalaiarasan, and K. S. Raj, "Mutual coupling reduction in microstrip patch antenna arrays using parallel coupled-line resonators," *IEEE Trans. Antennas Propag.*, vol. 66, no. 6, pp. 3188–3191, Jun. 2018.

[6] K. L. Chung and S. Kharkovsky, "Mutual coupling reduction and gain enhancement using angular offset elements in circularly polarized patch array," *IEEE Trans. Antennas Propag.*, vol. 62, no. 4, pp. 2176–2180, Apr. 2014.

[7] L. Liu, S. W. Cheung, and T. I. Yuk, "Compact MIMO antenna for portable devices in UWB applications," *IEEE Trans. Antennas Propag.*, vol. 61, no. 8, pp. 4257–4264, Aug. 2013.

[8] L. Wang, Y. Liu, L. Zhang, Y. Liu, and B. Wang, "Compact UWB MIMO antenna with high isolation using fence-type decoupling structure," *IEEE Trans. Antennas Propag.*, vol. 68, no. 2, pp. 1272–1276, Feb. 2020.

[9] J. Sui and K.-L. Wu, "Self-curing decoupling technique for two inverted-F antennas with capacitive loads," *IEEE Trans. Antennas Propag.*, vol. 66, no. 3, pp. 1093–1101, Mar. 2018.

[10] K.-C. Lin, C.-H. Wu, C.-H. Lai, and T.-G. Ma, "Novel dual-band decoupling network for two-element closely spaced array using synthesized microstrip lines," *IEEE Trans. Antennas Propag.*, vol. 60, no. 11, pp. 5118–5128, Nov. 2012.

[11] X.-J. Zou, G.-M. Wang, Y.-W. Wang, and H.-P. Li, "An efficient decoupling network between feeding points for multielement linear arrays," *IEEE Trans. Antennas Propag.*, vol. 67, no. 5, pp. 3101–3108, May 2019.

[12] C.-H. Wu, C.-L. Chiu, and T.-G. Ma, "Very compact fully lumped decoupling network for a coupled two-element array," *IEEE Trans. Antennas Propag.*, vol. 64, no. 2, pp. 751–755, Feb. 2016.

[13] F. Yang and Y. Rahmat-Samii, "Microstrip antennas integrated with electromagnetic band-gap (EBG) structures: A low mutual coupling design for array applications," *IEEE Trans. Antennas Propag.*, vol. 51, no. 10, pp. 2936–2946, Oct. 2003.

[14] A. Khan, Y. He, Z. He, and Z. N. Chen, "A compact quadruple-band circular polarized MIMO antenna with low mutual coupling," *IEEE Trans. Circuits Syst. II, Exp. Briefs*, vol. 70, no. 2, pp. 501–505, Feb. 2023.

[15] K. Wei, J.-Y. Li, L. Wang, Z.-J. Xing, and R. Xu, "Mutual coupling reduction by novel fractal defected ground structure bandgap filter," *IEEE Trans. Antennas Propag.*, vol. 64, no. 10, pp. 4328–4335, Oct. 2016.

[16] S. Zhang and G. F. Pedersen, "Mutual coupling reduction for UWB MIMO antennas with a wideband neutralization line," *IEEE Antennas Wireless Propag. Lett.*, vol. 15, pp. 166–169, 2016.

[17] M.-C. Tang et al., "Mutual coupling reduction using meta-structures for wideband, dual-polarized, and high-density patch arrays," *IEEE Trans. Antennas Propag.*, vol. 65, no. 8, pp. 3986–3998, Aug. 2017.

[18] J. Li, S. Yang, Y. Gou, J. Hu, and Z. Nie, "Wideband dual-polarized magnetically coupled patch antenna array with high port isolation," *IEEE Trans. Antennas Propag.*, vol. 64, no. 1, pp. 117–125, Jan. 2016.

[19] A. Khan, Y. He, and Z. N. Chen, "An eight-port circularly polarized wideband MIMO antenna based on a metamaterial-inspired element for 5G mmWave applications," *IEEE Antennas Wireless Propag. Lett.*, vol. 22, no. 7, pp. 1572–1576, Jul. 2023.

[20] Z. Niu, H. Zhang, Q. Chen, and T. Zhong, "Isolation enhancement in closely coupled dual-band MIMO patch antennas," *IEEE Antennas Wireless Propag. Lett.*, vol. 18, no. 8, pp. 1686–1690, Aug. 2019.

[21] T. Hassan, M. U. Khan, H. Attia, and M. S. Sharawi, "An FSS based correlation reduction technique for MIMO antennas," *IEEE Trans. Antennas Propag.*, vol. 66, no. 9, pp. 4900–4905, Sep. 2018.

[22] M. Akbari, M. M. Ali, M. Farahani, A. R. Sebak, and T. Denidni, "Spatially mutual coupling reduction between CP-MIMO antennas using FSS superstrate," *Electron. Lett.*, vol. 53, no. 8, pp. 516–518, Apr. 2017.

[23] F.-M. Yang, L. Peng, X. Liao, K.-S. Mo, X. Jiang, and S.-M. Li, "Coupling reduction for a wideband circularly polarized conformal array antenna with a single-negative structure," *IEEE Antennas Wireless Propag. Lett.*, vol. 18, no. 5, pp. 991–995, May 2019.

[24] K. Wei and B.-C. Zhu, "The novel W parasitic strip for the circularly polarized microstrip antennas design and the mutual coupling reduction between them," *IEEE Trans. Antennas Propag.*, vol. 67, no. 2, pp. 804–813, Feb. 2019.

[25] F. Liu, J. Guo, L. Zhao, G.-L. Huang, Y. Li, and Y. Yin, "Dual-band metasurface-based decoupling method for two closely packed dual-band antennas," *IEEE Trans. Antennas Propag.*, vol. 68, no. 1, pp. 552–557, Jan. 2020.

[26] Y. Zhang, Y. Li, M. Hu, P. Wu, and H. Wang, "Dual-band circular-polarized microstrip antenna for ultrawideband positioning in smartphones with flexible liquid crystal polymer process," *IEEE Trans. Antennas Propag.*, vol. 71, no. 4, pp. 3155–3163, Apr. 2023.

[27] W. Zhang, Y. Li, K. Wei, and Z. Zhang, "Dual-band decoupling for two back-to-back PIFAs," *IEEE Trans. Antennas Propag.*, vol. 71, no. 3, pp. 2802–2807, Mar. 2023.

[28] J.-H. Xun, L.-F. Shi, W.-R. Liu, G.-X. Liu, and S. Chen, "Compact dual-band decoupling structure for improving mutual coupling of closely placed PIFAs," *IEEE Antennas Wireless Propag. Lett.*, vol. 16, pp. 1985–1989, 2017.

[29] C. Wang, H. Wang, P. Wu, and M. Hou, "Dual-band closed-slot MIMO antenna for terminal wireless applications," *IEEE Trans. Antennas Propag.*, vol. 70, no. 8, pp. 6514–6525, Aug. 2022.

[30] M. Li, Y. Zhang, D. Wu, K. L. Yeung, L. Jiang, and R. Murch, "Decoupling and matching network for dual-band MIMO antennas," *IEEE Trans. Antennas Propag.*, vol. 70, no. 3, pp. 1764–1775, Mar. 2022.

[31] P. Garg and P. Jain, "Isolation improvement of MIMO antenna using a novel flower shaped metamaterial absorber at 5.5 GHz WiMAX band," *IEEE Trans. Circuits Syst. II, Exp. Briefs*, vol. 67, no. 4, pp. 675–679, Apr. 2020.

Asif Khan received the bachelor's degree in telecommunication engineering from Hazara University, Mansehra, Pakistan, in 2018, and the M.S. degree in electrical engineering from North China Electric Power University, Beijing, China, in 2021. He is currently pursuing the Ph.D. degree in information and communications engineering with Shenzhen University, Shenzhen, China.

His current research interests include mobile terminal antennas, multiple-input multiple-output (MIMO) antennas, shared-radiator antennas, millimeter-wave antennas, and meta-antennas.

Yejun He (Senior Member, IEEE) received the Ph.D. degree in information and communication engineering from the Huazhong University of Science and Technology (HUST), Wuhan, China, in 2005.

From 2005 to 2006, he was a Research Associate with the Department of Electronic and Information Engineering, The Hong Kong Polytechnic University, Hong Kong. Since 2006, he has been a Faculty of Shenzhen University, Shenzhen, China, where he is currently a Full Professor with the College of Electronics and Information Engineering, the Director of the Sino-British

Antennas and Propagation Joint Laboratory of Ministry of Science and Technology of the People's Republic of China (MOST), the Director of the Guangdong Engineering Research Center of Base Station Antennas and Propagation, and the Director of the Shenzhen Key Laboratory of Antennas and Propagation. From 2006 to 2007, he was a Research Associate with the Department of Electronic Engineering, Faculty of Engineering, The Chinese University of Hong Kong, Hong Kong. In 2012, he joined the Department of Electrical and Computer Engineering, University of Waterloo, Waterloo, ON, Canada, as a Visiting Professor. From 2013 to 2015, he was an Advanced Visiting Scholar (Visiting Professor) with the School of Electrical and Computer Engineering, Georgia Institute of Technology, Atlanta, GA, USA. From 2023 to 2024, he is an Advanced Research Scholar (Visiting Professor) with the Department of Electrical and Computer Engineering, National University of Singapore, Singapore. He has authored or coauthored more than 300 refereed journal and conference papers and seven books. He holds about 20 patents. His research interests include wireless communications, antennas, and radio frequency.

Dr. He is a fellow of IET and a Senior Member of the China Institute of Communications and the China Institute of Electronics. He was a recipient of the Shenzhen Overseas High-Caliber Personnel Level B (Peacock Plan Award B) and the Shenzhen High-Level Professional Talent (Local Leading Talent). He received the Second Prize of Shenzhen Science and Technology Progress Award in 2017, the Three Prize of Guangdong Provincial Science and Technology Progress Award in 2018, and the Second Prize of Guangdong Provincial Science and Technology Progress Award in 2023. He was selected as the Pengcheng Scholar Distinguished Professor, Shenzhen, and the Minjiang Scholar Chair Professor of Fujian Province, China, in 2020 and 2022, respectively. He is currently the Chair of IEEE Antennas and Propagation Society-Shenzhen Chapter and obtained the 2022 IEEE APS Outstanding Chapter Award. He has served as a Technical Program Committee Member or a Session Chair for various conferences, including the IEEE Global Telecommunications Conference (GLOBECOM), the IEEE International Conference on Communications (ICC), the IEEE Wireless Communication Networking Conference (WCNC), and the IEEE Vehicular Technology Conference (VTC). He served as the TPC Chair for IEEE ComComAp 2021 and the General Chair for IEEE ComComAp 2019. He was selected as a Board Member of the IEEE Wireless and Optical Communications Conference (WOCC). He served as the TPC Co-Chair for WOCC 2023/2022/2019/2015, APCAP 2023, UCMMT 2023, ACES-China2023, NEMO 2020, and so on. He acted as the Publicity Chair of several international conferences such as IEEE PIMRC 2012. He is serving as an Executive Chair of 2024 IEEE International Workshop of Radio Frequency and Antenna Technologies. He is a Principal Investigator for over 40 current or finished research projects, including the National Natural Science Foundation of China, Ministry of Science and Technology of the People's Republic of China (MOST), the Science and Technology Program of Guangdong Province, and the Science and Technology Program of Shenzhen City. He has served as a reviewer for various journals, such as IEEE TRANSACTIONS ON VEHICULAR TECHNOLOGY, IEEE TRANSACTIONS ON COMMUNICATIONS, IEEE TRANSACTIONS ON INDUSTRIAL ELECTRONICS, IEEE TRANSACTIONS ON ANTENNAS AND PROPAGATION, IEEE WIRELESS COMMUNICATIONS, IEEE COMMUNICATIONS LETTERS, *International Journal of Communication Systems*, and *Wireless Personal Communications*. He is serving as an Associate Editor for IEEE TRANSACTIONS ON ANTENNAS AND PROPAGATION, IEEE TRANSACTIONS ON MOBILE COMPUTING, *IEEE Antennas and Propagation Magazine*, IEEE ANTENNAS AND WIRELESS PROPAGATION LETTERS, *International Journal of Communication Systems*, *China Communications*, and *ZTE Communications*.

Zhi Ning Chen (Fellow, IEEE) received the B.Eng., M.Eng., and Ph.D. degrees in electrical engineering from the Institute of Communications Engineering (ICE), Nanjing, China, in 1985, 1988, and 1993, respectively, and the Ph.D. degree from the University of Tsukuba, Tsukuba, Japan, in 2003.

From 1988 to 1995, he worked at ICE as a Lecturer and later a Professor, and at Southeast University, Nanjing, as a Post-Doctoral Fellow and later an Associate Professor. From 1995 to 1997, he worked at the City University of Hong Kong (HK), Hong Kong, as a Research Assistant and later a Research Fellow. From 1997 to 1999, he conducted his research at the University of Tsukuba, with the Japan Society for the Promotion of Science (JSPS) Fellowship Award. From 1999 to 2016, he worked at the Institute for Infocomm Research (formerly the Center for Wireless Communications), National University of Singapore, Singapore, as a Principal Scientist, the Department Head and Manager, and a Technical Advisor. In 2001 and 2004, he visited the University of Tsukuba twice under the JSPS Fellowship Program (senior level). In 2004, he worked at the IBM Thomas J. Watson Research Center, Yorktown Heights, NY, USA, as an Academic Visitor. In 2012, he joined the Department of Electrical and Computer Engineering, National University of Singapore, as a tenured Full Professor, where he is currently a Provost Chair Professor, and the Founder and the Director of the Advanced Research and Technology Innovation Center. In 2013, he visited Laboratoire des SignauxetSystmes, UMR8506 CNRS-Supelec, Paris-Sud University, Gif-sur-Yvette, France, as a Senior DIGITEO Guest Scientist. In 2015, he visited the Center for Northeast Asian Studies, Tohoku University, Sendai, Japan, as a Senior Visiting Professor. He has provided 12 local and overseas companies with technical consultancy services as a Technical Advisor, a Guest Professor, and a Chief Scientist. He has published more than 680 academic articles and six books titled *Broadband Planar Antennas* (Wiley, 2005), *UWB Wireless Communication* (Wiley, 2006), *Antennas for Portable Devices* (Wiley, 2007), *Antennas for Base Stations in Wireless Communications* (McGraw-Hill, 2009), *Handbook of Antenna Technologies* (with 76 chapters) (Springer References, 2016, as the Editor-in-Chief), and *Substrate-Integrated Millimeter-Wave Antennas for Next-Generation Communication and Radar Systems* (Wiley and IEEE Press Series on Electromagnetic Wave Theory, 2021). He holds 35 granted and filed patents, and completed more than 43 technology-licensed deals with the industry. He is pioneering in developing small and wideband and ultrawideband antennas, wearable and implanted medical antennas, package antennas, near-field antennas and coils, 3-D integrated low-temperature co-fired ceramic (LTCC) arrays, microwave lens antennas, microwave metamaterial-metasurface antennas for communications, sensing, and imaging systems. He is more interested in the translational research of electromagnetic metamaterials and the applications of characteristic mode analysis, transformation optics, and prior-knowledge-guided deep learning-enabled optimization and generative design methods to antenna engineering.

Dr. Chen has served as a member for the Fellow Committee and the New Direction Committee. He is also serving as a member for the IEEE APS AdCom and the IEEE Future Networks Initiative Technology Focus Editorial Board. He is also a member of the State Key Laboratory of Millimeter Waves, Southeast University, and the State Key Laboratory of Terahertz and Millimeter Waves, City University of Hong Kong. He was elevated to a fellow of the Academy of Engineering, Singapore, in 2019, and a fellow and the Vice President of the Asia-Pacific Artificial Intelligence Association. He has also served as a reviewer for local and overseas research organizations in Canada, Chile, China mainland, HK SAR, Finland, Ireland, Sweden, and the U.K. He was a recipient of the IEEE Antennas and Propagation Society (APS) John Kraus Antenna Award in 2021, the Best Paper Award at the International Symposium on Antennas and Propagation in 2010, the CST University Publication Awards in 2008 and 2015, the ASEAN Outstanding Engineering Achievement Award in 2013, the Institution of Engineers Singapore Prestigious Engineering Achievement Awards in 2006 and 2013 (two awards), and more than 28 academic awards by the students under his supervision. He was the Founding General Chair of the Marina Forum (MarFor in 2021), the International Workshop on Antenna Technology (iWAT in 2005), the International Symposium on InfoComm and Mechatronics Technology in Biomedical and Healthcare Application (IS 3T-in-3A in 2010), the International Microwave Forum (IMWF in 2010), and the Asia-Pacific Conference on Antennas and Propagation (APCAP in 2012). He has also been involved in multiple international events as the General Chair, the Chair, and a member of program committees and advisory committees. He was the General Chair of the 2021 IEEE International Symposium on Antennas and Propagation and the USNC-URSI Radio Science Meeting (the first version out of North America). He has been invited to deliver more than 190 keynote, plenary, and invited speeches at international academic and industrial events. He has been serving on the IEEE Council on RFID as a Distinguished Lecturer since 2016, where he served as the Founding Vice President from 2015 to 2020. He has severed as an Associate Editor for IEEE TRANSACTIONS ON ANTENNAS AND PROPAGATION and a Distinguished Lecturer for IEEE APS.